

Article

Application of Neural Network Algorithms for Central Wavelength Determination of Fiber Optic Sensors

Timur Agliullin ¹, Vladimir Anfinogentov ¹, Rustam Misbakhov ², Oleg Morozov ^{1,*}, Aydar Nasybullin ³, Airat Sakhabutdinov ¹ and Bulat Valeev ¹

¹ Department of Radiophotonics and Microwave Technologies, Kazan National Research Technical University Named after A.N. Tupolev-KAI, 10 K. Marx St., Kazan 420111, Russia; taagliullin@kai.ru (T.A.); vianfinogentov@kai.ru (V.A.); azhsakhabutdinov@kai.ru (A.S.); kje.student@mail.ru (B.V.)

² Almetyevsk Branch, Kazan National Research Technical University Named after A.N. Tupolev-KAI, 9b Stroiteli Avenue, Almetyevsk 423400, Russia; rushmisbakhov@kai.ru

³ Department of Design and Technology of Electronic Means, Kazan National Research Technical University Named after A.N. Tupolev-KAI, 10 K. Marx St., Kazan 420111, Russia; arnasybullin@kai.ru

* Correspondence: microoil@mail.ru

Featured Application: Interrogation systems of fiber-optic sensors.

Abstract: Fiber Bragg gratings are sensitive elements in fiber optic sensor networks, and this paper discusses the practicalities of using neural network algorithms to determine their central wavelengths. The problem is to determine the central wavelength of a single sensor, the parameters of which are obtained using a low-resolution spectrum analyzer. The configuration of the neural network and the algorithm for producing the training and control datasets are specified. The training results for the selected neural network configuration demonstrated that the proposed method could determine the position of the central wavelength with a resolution two and a half orders of magnitude higher than the resolution of the input data sampling. The obtained results demonstrate that the approach makes it possible to determine the FBG central wavelength shift with an error not exceeding ~0.5 pm at a spectrum analyzer resolution of 167 pm.

Keywords: spectrum shift determination; neural network; stochastic optimization; Adam optimization method; artificial intelligence; fiber optics sensor; fiber Bragg gratings; central wavelength determination methods



Citation: Agliullin, T.; Anfinogentov, V.; Misbakhov, R.; Morozov, O.; Nasybullin, A.; Sakhabutdinov, A.; Valeev, B. Application of Neural Network Algorithms for Central Wavelength Determination of Fiber Optic Sensors. *Appl. Sci.* **2023**, *13*, 5338. <https://doi.org/10.3390/app13095338>

Academic Editor: Massimo Garai

Received: 21 March 2023

Revised: 22 April 2023

Accepted: 23 April 2023

Published: 24 April 2023



Copyright: © 2023 by the authors. Licensee MDPI, Basel, Switzerland. This article is an open access article distributed under the terms and conditions of the Creative Commons Attribution (CC BY) license (<https://creativecommons.org/licenses/by/4.0/>).

1. Introduction

Fiber optic sensor system design of the point and/or quasi-distributed type is impossible without solving the key problem for this type of system, which is finding the central wavelength in the reflection spectrum with the most accuracy. Thus, the shift of the central wavelength of a fiber optic sensor based on a resonant structure (a fiber Bragg grating (FBG) [1–3], a Fabry–Perot interferometer [4–6], or a ring resonator [7–10]) or other types of resonators [9,11] determines the magnitude of the physical impact. In addition, temperature [9,12,13], pressure [14,15], deformation [16,17], friction, wear, and other types of impacts [18,19] are all determined using information about the position of the sensing element's reflection spectrum.

The primary factor limiting the estimation accuracy of the physical impact magnitude in fiber optic sensor systems is the inadequate resolution of the devices used to measure the spectral properties of such sensors. Increasing the resolution of a device's built-in spectrum analyzer can improve its technical capabilities, but this usually comes at a cost that rises almost exponentially.

Diverse methods have been proposed to improve the precision of determining the position of the sensing elements' spectra. Thus, the sub-pixel spectrum processing tech-

niques [20–22] made it possible to increase the resolution by one or two orders of magnitude [23]. Meanwhile, after adjusting for the nonlinear spectrum distortions in charge-coupled devices depending on the signal accumulation time, the resolution can be improved by another order of magnitude but only in an extremely narrow frequency range [24]. Due to additional mathematical processing of the data, the maximum results obtained indicated that the physical resolution of the devices could be increased by nearly two orders of magnitude [23,24]. However, the achieved capabilities to determine the magnitude of the spectral shift are insufficient for some applications. The spectral shift can be determined with greater precision with the help of sensitive elements with narrow spectral characteristics. Fiber Bragg structures with discrete phase shifts, whose reflection spectra are an order of magnitude narrower than those of fiber Bragg gratings [25–27], and optical elements based on ring resonators, whose Fano resonance has a very narrow reflection spectrum [8,11,28], fall into this category of sensitive elements. However, high-resolution spectrum analyzers are also needed when working with sensitive elements that exhibit narrow spectral characteristics.

Microwave-photonic methods [20,29,30] are another way to improve the accuracy of measurements. These methods work by transferring the measurement process from the optical range of the electromagnetic spectrum to the microwave one. Although microwave-photonic methods are highly accurate for physical parameters determination, they do necessitate upgrading to new technologies and replacing the current hardware and software of measurement instruments.

A number of researchers have proposed the artificial intelligence algorithms to determine a central wavelength of sensors based on fiber Bragg gratings (Table 1). L. Negri et al. [31] proposed to use a fully connected (FCC, fully connected cascade) neural network trained by the Neuron-by-Neuron algorithm to approximate the FBG reflection spectrum and eliminate spectrum distortions, the spectra of which were obtained with a resolution of 1 pm. They managed to achieve an error in the FBG central wavelength determination of 1.45 pm using the approximation of the FBG spectrum curve using the neural network. Y. An et al. [32] used a feed-forward neural network (BPNN) with an L-M optimization algorithm to determine the temperature using FBG. Based on the experimental data of the FBG reflectance spectra, the achieved accuracy was 0.2081 °C (root-mean-square error, RMSE), 0.8943 °C (max absolute error) or 2.081 pm (RMSE), 8.943 pm (max absolute error) on the training set. A. Zimmermann et al. [33] used a neural network (ANN) with three FBG sensors and three photodetectors to expand the temperature measurement range (from 25 °C to 250 °C). The accuracy obtained was ± 0.4 °C (2σ , where σ is the standard deviation in normal distribution) or ± 4 pm up to 150 °C and ± 0.9 °C (2σ) or ± 9 pm above 150 °C. A. Paterno et al. [34] reported on the use of a network of radial basis functions for approximating the FBG reflectance spectrum. The neural network was trained according to the algorithm described by Orr [35]. Using the approximation of a spectrum consisting of 1000 points, an accuracy of 2 pm (mean error) and 25 pm (σ) was achieved on an interval of 4 nm.

Table 1. Accuracy of neural network methods for FBG interrogation.

Reference	Wavelength Estimation Error	Temperature Estimation Error	Data Resolution
[31]	1.45 pm (RMSE)	0.145 °C	1 pm
[32]	2.081 pm (RMSE)	0.2081 °C	-
[33]	2 pm (2σ)	0.2 °C	-
[34]	2 pm (mean), 25 pm (σ)	0.2 °C	4 pm
Current work	0.411 pm (MAE), 0.533 pm (σ)	0.05 °C	167 pm

In this work, in contrast to [31–34], we proposed to use a neural network of a simpler configuration to increase the processing speed of FBG sensors in the interval Δ under study, the spectra of which were taken at a low resolution of the spectrum analyzer (~ 167 pm/pixel), and the aim was the accuracy of the FBG central wavelength shift deter-

mination with an error not exceeding 1 pm. The obtained accuracy corresponded to 0.04 °C (mean absolute error, MAE) and 0.05 °C (σ). Looking ahead, we include in Table 1 the data obtained from our study to compare them with those of other researchers.

As the processing power of computers has increased over the past few decades, artificial neural networks and other machine-learning techniques have become widespread in all areas of science and technology. However, while many articles (e.g., [31,36–38]) demonstrate results when similar approaches are used, this does not exhaust the potential of artificial neural networks.

2. Problem Statement

In our situation, we were using an I-MON-512 Interrogation unit [24]. We assumed a fiber Bragg grating (FBG) with a length L ranging from 0.5 to 3.5 mm, a period Λ varying from 531.111 to 531.472 μm , and an induced refractive index n ranging from $0.5 \cdot 10^{-4}$ to $1.5 \cdot 10^{-4}$, which was subjected to a specific physical effect (stretching/compression, temperature, etc.) causing a shift of the FBG central wavelength. With such parameters, the FBG central wavelength λ_B ranged from 1549.5 to 1550.5 nm, and the full width at half maximum of the spectrum ranged from 0.229 to 1.458 nm. The broadband radiation from a superluminescent diode was directed to the FBG via a fiber optic circulator, and the I-MON-512 spectrum analyzer received the reflection spectrum. The left and right boundaries of the controlled spectral range were $\lambda_{\min} = 1510$ nm and $\lambda_{\max} = 1595$ nm, respectively; the number of points in the spectrum was $N = 510$; and the discretization interval was $\Delta\lambda = (\lambda_{\max} - \lambda_{\min})/N \approx 0.167$ nm.

Without knowing the true FBG central wavelength, the data collected from the I-MON-512 cannot be used as input data for the neural network model. So instead, we used a mathematical model based on the homogeneous layers method [39] and transfer matrices [40] to obtain the FBG spectra with pre-defined central wavelengths. Initially, the FBG reflection spectrum was formed based on a mathematical model using the mathematical apparatus of transfer matrices [40] or the homogeneous layers method [39]. Then, the discretization of the modeled spectrum was performed with an interval equal to that of the spectrum analyzer. The resulting data array was essentially a discrete spectrum similar to that obtained via the interrogation device, and at the same time, the exact value of its central wavelength was known. Thus, the mathematical modeling apparatus enabled precise comparisons between the discrete spectrum and the corresponding central wavelength. These were the datasets used to train the neural network.

The position of the FBG spectrum was studied in a controlled wavelength range $\lambda_B \pm \Delta/2$, at $\Delta = 3$ nm, which determined, taking into account the spectrum analyzer's resolution, the dimension of the neural network input data $M = \text{int}(\Delta/\Delta\lambda) + 1$. Within the scope of the problem just described, this range included 19 spectrum values, determining 19 input values of the neural network. The spectra of the same FBG for two different positions (red and blue lines) are schematically shown in Figure 1. The solid line shows the true FBG spectra (as if they were obtained with any arbitrarily small discretization interval), and the dots show the values of the spectra obtained discretely. Figure 1 uses the following designations: S^r and S^b are spectra at two positions; λ_i is the wavelength, λ_L is the wavelength of the left, and λ_{L+M-1} is the right boundary of the controlled part of the spectrum; $\Delta\lambda$ is the discretization interval; and \mathbf{D} is the relative shift vector of the spectrum (S^b vs. S^r), which is the same for all spectrum points.

To bring the mathematical model of the spectrum as close as possible to the actual physical spectrum, the model incorporated the noise component and the minimum threshold of the light response. The amplitude of the noise component a_N was assumed to be less than 0.2% of the maximum amplitude, and the minimum value in the FBG spectrum was assumed to be less than 20% of the maximum amplitude.

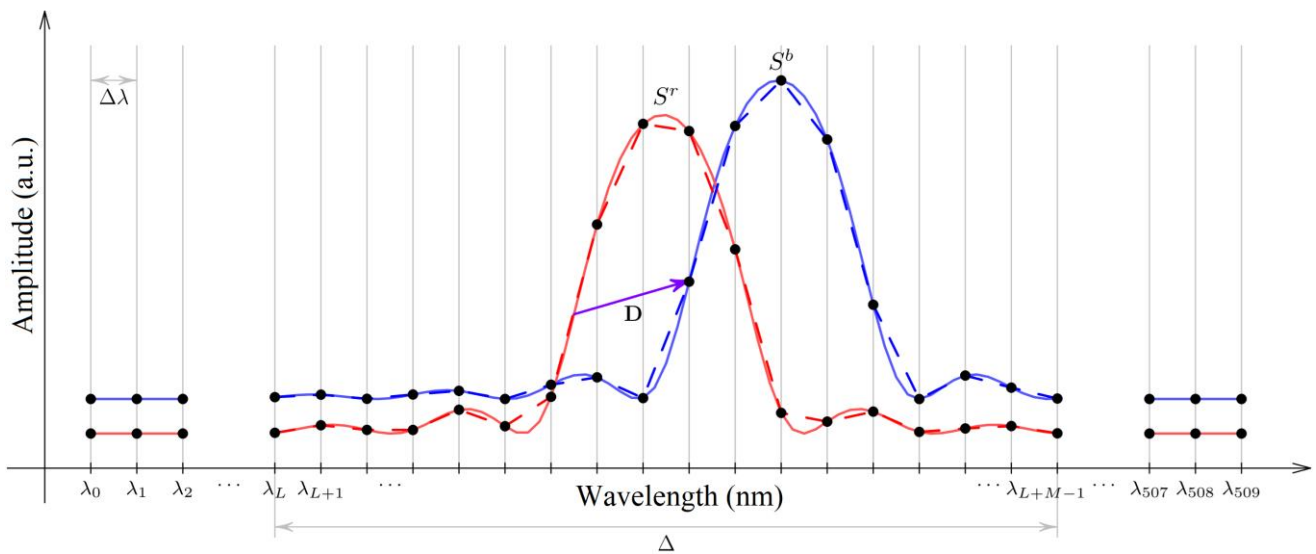


Figure 1. A diagram of the same FBG spectrum in two positions. The red line represents the unperturbed state, while the blue line represents the shifted state; dotted lines denote the discretized spectrum, and solid lines denote the true (continuous) spectrum.

To make the solution of to the problem universally applicable, let us replace the variables:

$$\tilde{\lambda}_i = \frac{\lambda_i - \lambda_L}{\lambda_{L+M-1} - \lambda_L}, \quad \tilde{R}_i = \frac{R_i - \min(\mathbf{R})}{\max(\mathbf{R}) - \min(\mathbf{R})}, \quad (1)$$

thus moving the input data into the range of amplitude and wavelength variation from 0 to 1. In Equation (1), the set \mathbf{R} denotes the set of reflection coefficients $R_i, i = 0.509$, belonging to the wavelength range $\lambda \in [1510, 1595]$ nm. Let us omit the tilde sign for normalized data to make future recording easier. We also assume that we are dealing with normalized values by default.

The normalization of the spectrum values by wavelength and amplitude enabled us to make the solution universal and apply it to FBG wavelength determination in any frequency range, assuming the similarity criterion was met.

An elementary dataset is a collection of M normalized discrete values of the spectrum $\{R_i\} (i = 0, M - 1)$ obtained through mathematical modeling. The target value of the central wavelength λ_B corresponds to this dataset.

As a neural network, we used one of the most commonly used architectures in data approximation, linear and nonlinear regression problems—a three-layer Rosenblatt’s perceptron with variable S-A connections [41]. The three layers were sensory S (input), associative A (hidden), and response R (output). A distinguishing feature of Rosenblatt’s perceptron with sequential links is the synaptic connectivity of each neuron of the current layer with all neurons of the next layer [41]. Only associative and response layers can be trained in this configuration. The computational model used in this problem was configured from 19 elements of the sensory layer, 10 elements of the associative layer, and one element of the response layer, as shown in Figure 2.

The computational difficulty of the proposed neural network can be estimated by counting the number of multiplication and addition operations required. For example, the direct signal propagation algorithm through the neural network can be estimated as $(n - 1)$ matrix multiplications and $(n - 1)$ vector additions, where n is the number of model layers. Therefore, the multiplicative computational complexity of the algorithm is defined as $O(w)$, and the arithmetic complexity is of the order $O(2w + v)$, where w is the number of synaptic connections and v is the number of neuron shifts equal to the number of neurons of the associative and response layers. Thus, for the neural network used, the computational

complexity was $O(288)$. This value ensures near-instantaneous network response, which is especially important when running real-time sensor systems.

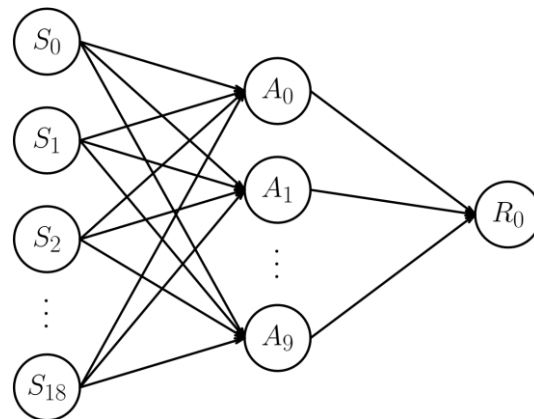


Figure 2. Computational model of a three-layer Rosenblatt's perceptron.

The problem was simplified to calculating the true FBG center wavelength with an error less than $\sim \Delta\lambda \cdot 10^{-3}$, having only spectrum data $\{\lambda_i, R_i\}$ ($i = 0, M - 1$).

3. Parameter Selection

A significant problem, which influences the neural network training speed and convergence of the neural network response to the target function, is the choice of method for optimizing the network parameters, the activation function of neurons, and the choice of a criterion for evaluating the result (the loss minimization function). Modern optimization methods in linear and nonlinear regression and approximation problems use two main methods for minimizing the loss function: the stochastic gradient descent method [42] with its varieties and the accelerated Nesterov gradient method (the pulse accumulation method) [43]. Each ensures that the neural network training procedure quickly converges to the target value (target function).

The Adam optimization method [44] was used in this paper, combining the ideas of momentum accumulation and adaptive learning rate for each parameter. In addition to momentum accumulation, the algorithm considered the average non-centered variance of the gradients, which reduced the number of iterations required to converge the algorithm while improving the neural network's prediction accuracy. The Adam algorithm is distinguished by using exponential moving averages for gradients and their squares, controlled by the parameters β_1 (for the gradient) and β_2 (for the gradient square). Selecting these averages determines the speed and accuracy of algorithm convergence. To solve the problem empirically, the values $\beta_1 = 0.99$ and $\beta_2 = 0.999$ were selected at the initial learning rate $\eta = 10^{-3}$.

Continuous differentiability is a general requirement for an activation function, which comes from the requirements of algorithms based on calculation of the loss function gradient. The selection of the activation function type is typically influenced by the nature of the problem to be solved, the input and output data types, and the desired outcome of the neural network model. A linear activation function, for example, involves solving a linearly separable problem that does not require the hidden layer of the neural network. Hidden layers in a neural network indicate that a nonlinear separable problem is being solved. Nonlinear activation functions, such as sigmoidal functions, ReLU (Rectified Linear Unit) and its numerous varieties (Leaky ReLU, PReLU, RReLU), exponential functions, and radial basis functions, are required for such problems. Because of its advantages, such as monotonicity, boundedness, and the presence of a section close to linear, the sigmoidal activation function is convenient to use for the problem formulated here:

$$f(x, \alpha) = \frac{1}{1 + e^{-\alpha x}}, \quad \forall \alpha > 0, \quad (2)$$

where the parameter $\alpha = 0.5$ corresponds to a large length of the nearly linear function section. In Equation (2), the parameter α is responsible for the slope of the linear section near the ordinate 0. At $\alpha = 0$, the sigmoid function turns into a line $y = 0.5$; for $\alpha = +\infty$, it turns into a threshold function. The choice of the parameter $\alpha = 0.5$, or another value close to 0, leads to an increase in the length of the “linear” section of the function, as a result of which the sigmoid function behaves like a linear function (in the working section), while maintaining its nonlinearity.

In turn, the mapping from the associative layer space to the response layer space is linear, meaning that the value of the response layer neuron is the weighted sum of the values of the associative layer neurons.

The Euclidean norm between the target vector and the neural network’s response vector is the way to tell if the network is getting closer to the target value:

$$d(\mathbf{p}, \mathbf{q}) = \sqrt{\sum_{i=0}^{K-1} (p_i - q_i)^2}, \tag{3}$$

where \mathbf{p} is the target vector, \mathbf{q} is the response vector of the neural network, and K is the dimension of the target vector \mathbf{p} .

4. Training

By using a mathematical model that generates real-time input data at each training phase, the accumulation of a collection of training and test data in computer memory can be avoided. Furthermore, this method eliminates the need to label training and test datasets. Parameters from the ranges listed in Table 2 were used to create a model of the input data.

Table 2. FBG reflection spectrum modeling parameters.

Parameters	Values	Normalized Values
FBG length (L)	0.5 ÷ 3.5 mm	-
Refractive index (n)	1.4586604	-
Induced refractive index (Δn)	$0.5 \cdot 10^{-4}$ ÷ $1.5 \cdot 10^{-4}$	-
Controlled wavelength interval (Δ)	1548.5 ÷ 1551.5 nm	0 ÷ 1
Central wavelength (λ_B)	1549.5 ÷ 1550.5 nm	0.333 ÷ 0.667
Discretization interval ($\Delta\lambda$)	0.16667 nm	1/18
Full width at half height	0.229 ÷ 1.458 nm	0.076 ÷ 0.486
Maximum amplitude	0.61×2^{16} a.u.	1
Amplitude variation range	$3.92 \cdot 10^{-4} \times 2^{16}$ ÷ 0.15×2^{16} a.u.	$6.42 \cdot 10^{-4}$ ÷ 0.26
Noise	$0 \div 2 \times 10^{-3} \times 2^{16}$ a.u.	0 ÷ 0.002
Pedestal	$0 \div 2 \times 10^{-1} \times 2^{16}$ a.u.	0 ÷ 0.2

The algorithm that underpins the neural network training process includes the series of steps below:

1. Modeling of the FBG reflection spectrum at a wavelength arbitrarily selected from the range $[\lambda_B - 0.5 \text{ nm}; \lambda_B + 0.5 \text{ nm}]$, where λ_B is the central value of the wavelength within the controlled wavelength interval Δ . The resulting spectrum $\{R_i\}$ is discretized at $\Delta\lambda$ intervals. The amplitude values $\{R_i\}$ and the central wavelength λ_B are normalized by (1).
2. Setting the initial values of synaptic weights and shifts:

$$w_{k,j}^n = \frac{1}{2} - \text{rnd}(1), \quad b_k^n = \frac{1}{2} - \text{rnd}(1). \tag{4}$$

3. Direct signal propagation through a neural network, consisting of these steps:
 - Calculating the weighted sum of the sensory layer neurons' values;
 - Calculating the associative layer values (using a nonlinear activation function);
 - Calculating the weighted sum of the associative layer's neurons' values;
 - Calculating the value of the neurons in the response layer (using a linear activation function) for each neuron in the associative and reacting layers.
 - Direct propagation yielding a normalized FBG central wavelength value representing neural network responses.
4. Reverse propagation of the error signal, consisting of these steps:
 - Calculating the error of the FBG central wavelength determination (the norm between the target value vector and the neural network response vector) according to the selected metric;
 - Calculating the error for each neural network parameter in sequence using the Adam optimization algorithm;
 - Correcting synaptic weights and model shifts.
5. Verifying that the training algorithm criterion meets the requirement:

$$\left| \frac{1}{I} \sum_{i=K-I}^{K-1} d(\lambda_B^i, \bar{\lambda}^i) - \frac{1}{I} \sum_{j=K-2I}^{K-I-1} d(\lambda_B^j, \bar{\lambda}^j) \right| < \varepsilon_1, \tag{5}$$

where $\lambda_B^{i(j)}$ and $\bar{\lambda}^{i(j)}$ are the target and calculated values of the FBG central wavelength at the $i(j)$ th iteration, I is the number of iterations for which averaging occurs, K is the number of training iterations, and ε_1 is an arbitrary predetermined small value.

The neural network training that had occurred before the criterion met the requirement (5) amounted to a little more than 10^6 training algorithm iteration cycles. Figure 3 shows the dependence of the absolute error in determining the FBG central wavelength found according to norm (3) on the number of training process cycles. The dependence in Figure 3 is plotted on a semi-logarithmic scale for better visualization. The error value begins to slow after 10^6 training cycles and stabilizes at around 0.525 pm.

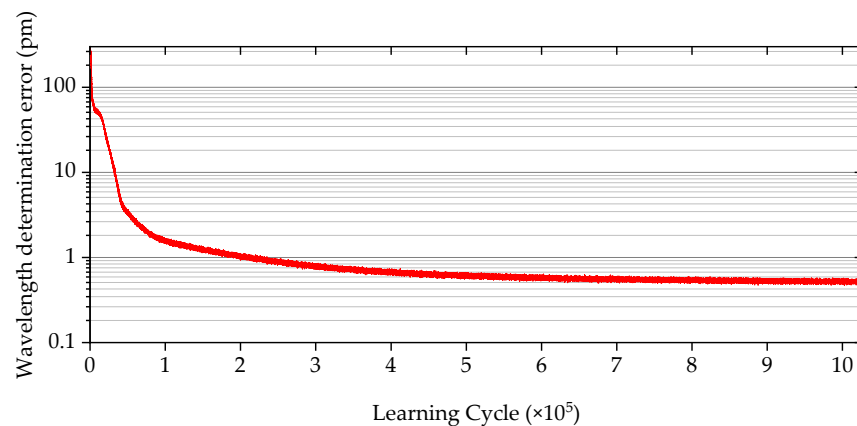


Figure 3. Absolute error in the FBG central wavelength determination depending on training cycles.

Neural network training generates a 10×19 matrix of weighting coefficients for the associative layer \mathbf{w}_A , a 1×10 matrix for the response layer \mathbf{w}_R , a 10×1 matrix for neuron shift vectors of associative \mathbf{b}_A layers, and a 1×1 matrix for neuron shift vectors of response \mathbf{b}_R layers.

The matrices of the weighting coefficients \mathbf{w}_A , \mathbf{w}_R , together with the shift vectors \mathbf{b}_A and \mathbf{b}_R , make it possible to determine the FBG reflection spectrum central wavelength

according to the decisive rule, using the values of the 19×1 FBG reflection spectrum \mathbf{R} as input data,

$$\bar{\lambda} = \mathbf{w}_R \times f(\mathbf{w}_A \times \mathbf{R} + \mathbf{b}_A, \alpha) + \mathbf{b}_R, \tag{6}$$

and ensure that the FBG central wavelength value is restored from the spectral data (Figure 4) obtained under low-resolution conditions.

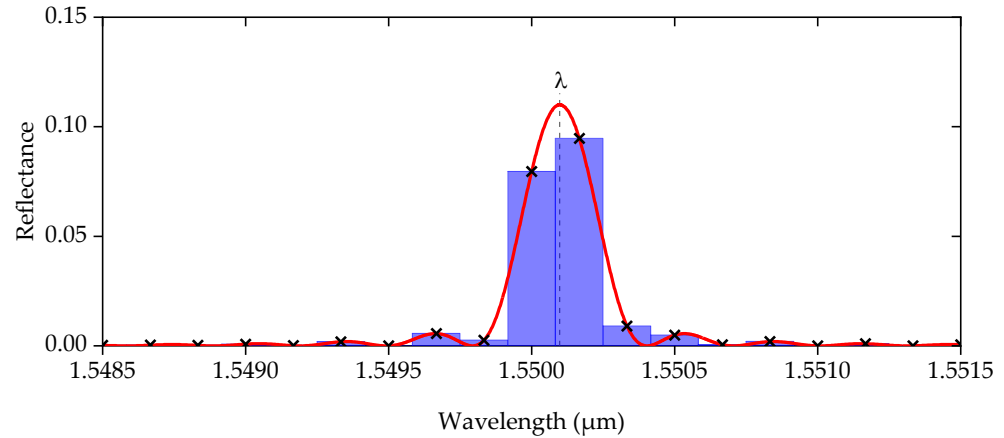


Figure 4. FBG spectral response: a bar chart at a discretization interval of 167 pm and a flat line at an infinitesimal discretization interval, where λ is the central wavelength.

5. Verification

To verify the neural network model, we used an algorithm consisting of a series of steps similar to the training algorithm, except for the error back propagation part of the algorithm:

1. Modeling of the FBG reflection spectrum at a wavelength arbitrarily selected from the range $[\lambda_B - 0.5 \text{ nm}; \lambda_B + 0.5 \text{ nm}]$, where λ_B is the central value of the wavelength within the controlled wavelength interval Δ . The resulting spectrum $\{R_i\}$ is discretized at $\Delta\lambda$ intervals. The amplitude values $\{R_i\}$ and the central wavelength λ_B are normalized using (1).
2. Calculation of the neural network response $\bar{\lambda}$ using (6).
3. Calculation of the error in FBG central wavelength determination using (3).

Figure 5 shows the neural network response’s dependence on the values of the FBG central wavelength λ for 10^4 iterations of the verification algorithm. The red line represents the dependence corresponding to the neural network model’s response; the blue line (along the additional axis) represents the magnitude of the error in the central wavelength determination $(\lambda - \bar{\lambda})$.

When the sensor system was in real-time operation, the profile of the FBG reflection spectrum serving as a sensor sensing element hardly changed. Consequently, it was intriguing to investigate the magnitude of the absolute error in determining the central wavelength that resulted from a plane-parallel shift of the same spectrum across the entire controlled wavelength section. Two approaches were of interest here. The first involved determining the FBG reflection spectrum central wavelength in the wavelength range with an interval Δ and fixed left λ_L and right λ_R boundaries. The second approach involved determining the FBG reflection spectrum central wavelength in the wavelength range with an interval Δ but with variable left λ_L and right λ_R boundaries. Here the boundary was determined according to a rule that ensured that the wavelength λ_{Max} corresponding to the maximum value in the discretely obtained spectrum $\lambda_{Max} = \max(\mathbf{R})$ was always located in the center of the wavelength range $[\lambda_L, \lambda_R]$. Figures 6 and 7 show the absolute errors in determining wavelengths using the first and second range control approaches, respectively.

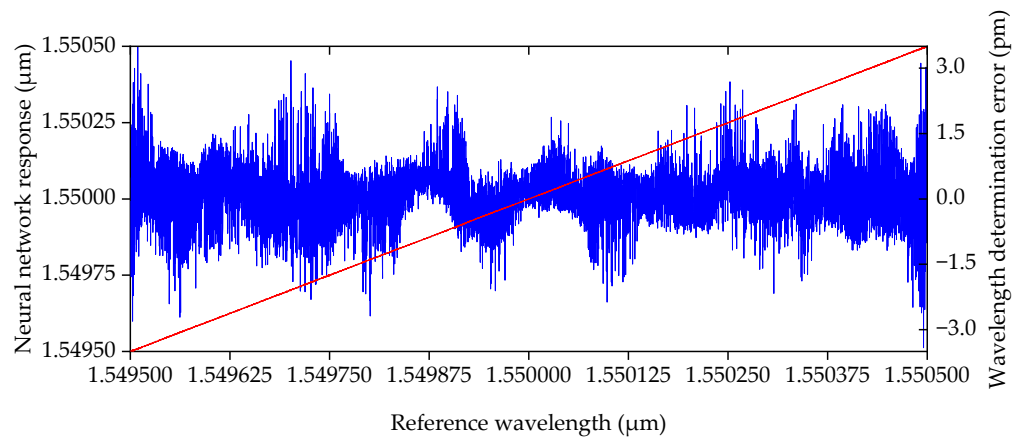


Figure 5. Dependence of the neural network response ($\bar{\lambda}$) on the FBG wavelength (λ) (red line) and absolute error in the wavelength determination ($\bar{\lambda} - \lambda$).

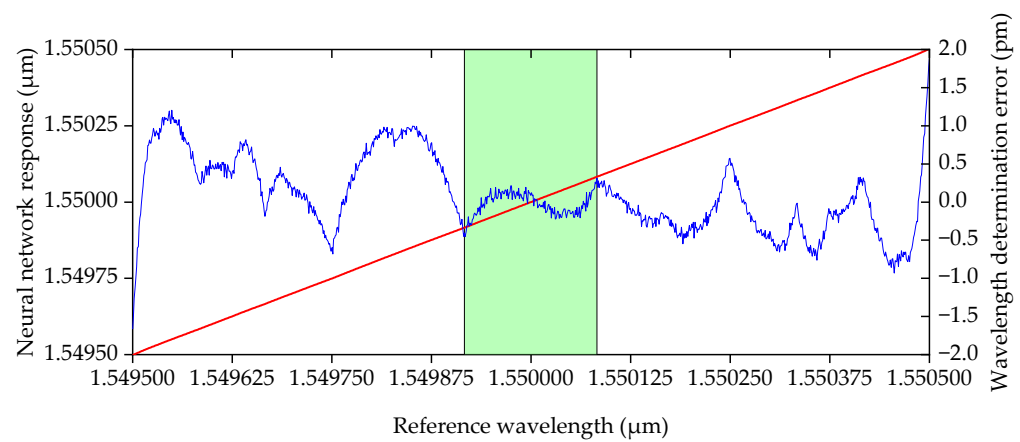


Figure 6. Error in determining the FBG central wavelength at a fixed-boundary interval.

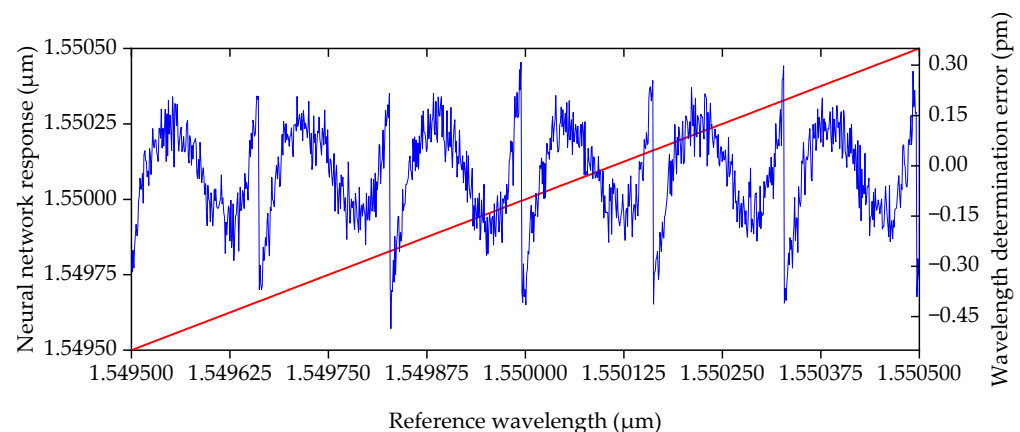


Figure 7. Error in determining the FBG central wavelength at a variable-boundary interval.

Comparing the errors in determining the central wavelength with fixed (Figure 6) and variable (Figure 7) boundaries revealed that the errors in the latter case were smaller and had an almost periodic dependence on the location of the FBG reflection spectrum maximum. It is also worth noting that the quasi-periodic dependence of errors in Figure 7 was caused by the errors belonging to the interval [1549.917, 1550.083] nm in Figure 6 (green area).

The distribution density of errors in determining the FBG central wavelength for each approach (fixed and variable boundaries) is shown in Figures 8 and 9, respectively.

In addition, the value of the FBG central wavelength error corresponding to the central wavelength shift for λ_B is plotted on the abscissa axis (on the additional ordinate axis).

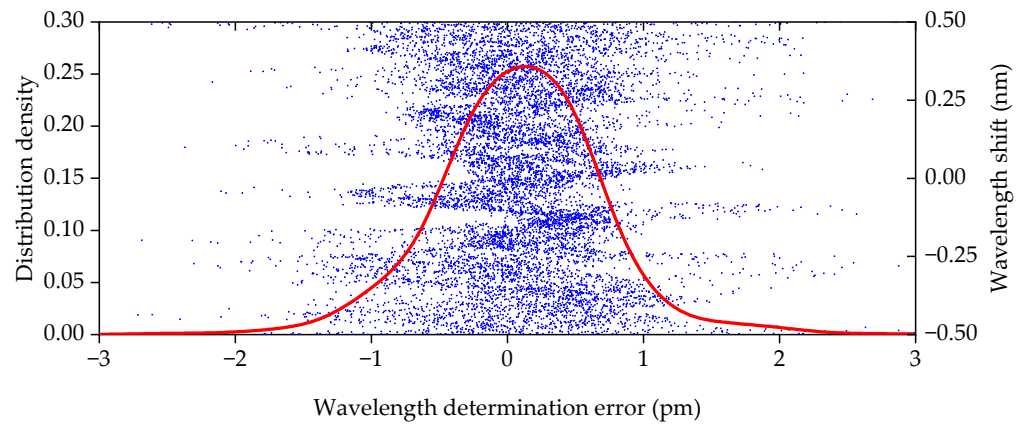


Figure 8. Distribution density of errors in determining the FBG central wavelength d_i at a fixed-boundary interval.

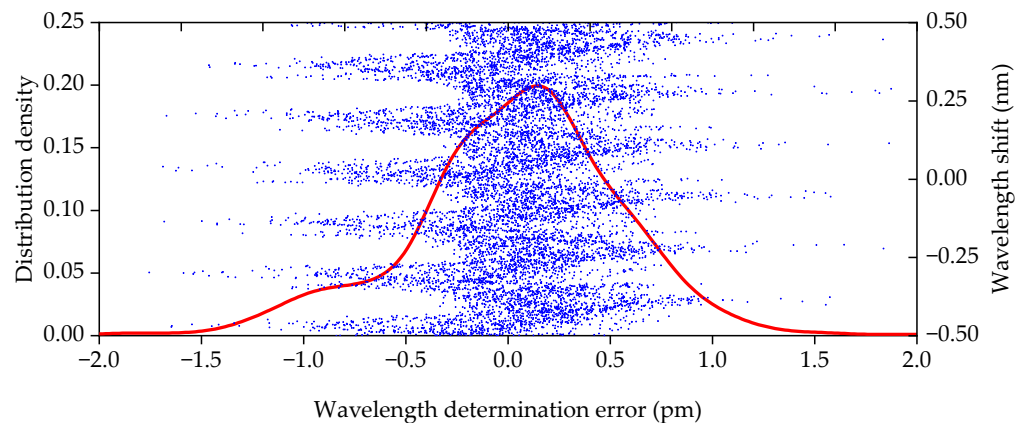


Figure 9. Distribution density of errors in determining the FBG central wavelength d_i at a variable-boundary interval.

The distribution of errors for both wavelength range boundary selection approaches was close to the normal distribution. For the fixed-boundary approach, the mathematical expectation was $\mu = 0.084$ pm, and the standard deviation was $\sigma = 0.627$ pm, with most of the error values (lower and upper quartiles) belonging to the interval $[-0.28, 0.46]$ pm. For variable boundaries, the mathematical expectation was $\mu = 0.045$ pm, and the standard deviation was $\sigma = 0.528$ pm, with most error values belonging to the interval $[-0.24, 0.39]$ pm. The statistical characteristics of the error distribution in calculating the central wavelength are shown in Table 3.

Table 3. Statistical characteristics of the error distribution.

Characteristic	Value (Fixed Boundaries)	Value (Variable Boundaries)
Mathematical expectation	0.084 pm	0.041 pm
Average absolute error	0.478 pm	0.411 pm
Median	0.097 pm	0.066 pm
Standard deviation	0.627 pm	0.533 pm

6. Conclusions

The results demonstrated that a neural network based on a three-layer Rosenblatt’s perceptron could be successfully applied in fiber optic sensor problems, specifically when

it was necessary to determine the central wavelength shift of a fiber Bragg grating used as a sensing element in a discrete sensor. The proposed method of employing a neural network had the advantages of requiring no complex calculations in the measurement mode and being implementable on simple microcontrollers. Furthermore, significant computational complexity was only incurred once during neural network training. During training, the proposed method transformed the spectrum values into dimensionless variables by shifting the coordinate axis. Once the calculations were completed, the dimensionless variables were converted back into dimensional values. This enabled a trained neural network to determine the FBG central wavelength across a broad range of wavelengths and for varying-quality FBGs. The suggested algorithm increased the resolution of wavelength shift determination by almost three orders of magnitude compared with the initial resolution of the spectrum analyzer, while maintaining the mathematical framework's apparent simplicity. This ensured that a spectrum analyzer with a 0.167 nm resolution could determine the shift of the fiber Bragg grating spectrum with an error of no more than 0.5 pm, which further determined the resolution when measuring, for instance, a temperature of 0.05 °C. The advantages of the method included its independence from broadband light source power fluctuations and the ability to determine the central wavelengths of the FBGs with different quality factors and in different spectral ranges using a neural network trained only once.

The spectra used for training suggest apodized FBGs whose side lobes are suppressed, which corresponds to physically formed FBGs according to Lloyd's recording scheme. Point-by-point writing [45,46] implies the possibility of recording non-apodized FBGs and FBGs of an arbitrary structure. The use of a neural network to determine the central wavelengths of structured FBGs or FBGs with phase or other inhomogeneities requires additional research. At the same time, the results obtained in this study make it possible to determine with certainty the center of wavelengths of non-overlapping apodized FBGs.

The main limitation of the proposed method was the impossibility of the central wavelength determination of the FBG with FWHM of less than 200 pm (~1.5 larger than the spectrum resolution). This limitation was due to the fact that when FWHM was less than the specified value, the FBG reflection spectrum obtained by the I-MON-512-based interrogator had one to two value points, which did not allow the determination of the value of the central wavelength with a given (required) accuracy. At the same time, there was a limitation in the impossibility of determining the central wavelength of the FBG with FWHM greater than the specified interval for finding the FBG ($\Delta = 3$ nm). The third limitation was the impossibility of determining the central wavelengths of two or more FBGs in the wavelength section under consideration ($\Delta = 3$ nm).

It must be noted that the second constraint is not a fundamental limitation of the proposed method, and in order to mitigate it, it is enough to retrain the neural network for a wider interval. The first limitation, however, can be removed only by increasing the physical resolution of the spectrum analyzer. Further research will be dedicated to the development of approaches for the central wavelength determination of two or more FBGs with overlapping spectra.

Author Contributions: Conceptualization, V.A. and A.S.; methodology, A.S. and A.N.; software, B.V. and A.S.; validation, T.A., R.M., and B.V.; formal analysis, V.A.; investigation, T.A., A.S., and B.V.; resources, O.M.; data curation, A.S.; writing—original draft preparation, B.V.; writing—review and editing, T.A., R.M., A.N., and A.S.; visualization, B.V.; supervision, O.M.; project administration, A.S.; funding acquisition, O.M. All authors have read and agreed to the published version of the manuscript.

Funding: This work was financially supported by the Ministry of Science and Higher Education as part of the "Priority 2030" program.

Institutional Review Board Statement: Not applicable.

Informed Consent Statement: Not applicable.

Data Availability Statement: The data presented in this study are available on request from the corresponding author.

Conflicts of Interest: The authors declare no conflict of interest.

References

1. Grattan, L.S.; Meggitt, B.T. (Eds.) *Optical Fiber Sensor Technology: Advanced Applications—Bragg Gratings and Distributed Sensors*; Springer: Boston, MA, USA, 2000; ISBN 978-0-7923-7946-1.
2. Kronenberg, P.; Rastogi, P.K.; Giaccari, P.; Limberger, H.G. Relative humidity sensor with optical fiber Bragg gratings. *Opt. Lett.* **2002**, *27*, 1385–1387. [[CrossRef](#)]
3. Tai, H. Theory of fiber optical Bragg grating: Revisited. In Proceedings of the Optical Modeling and Performance Predictions, San Diego, CA, USA, 6–7 August 2003; SPIE: Bellingham, DC, USA, 2004; Volume 5178, pp. 131–138.
4. Njegovec, M.; Donlagic, D. A Fiber-Optic Gas Sensor and Method for the Measurement of Refractive Index Dispersion in NIR. *Sensors* **2020**, *20*, 3717. [[CrossRef](#)] [[PubMed](#)]
5. Tseng, S.-M.; Chen, C.-L. Optical fiber Fabry-Perot sensors. *Appl. Opt.* **1988**, *27*, 547–551. [[CrossRef](#)] [[PubMed](#)]
6. Chen, P.; Dai, Y.; Zhang, D.; Wen, X.; Yang, M. Cascaded-Cavity Fabry-Perot Interferometric Gas Pressure Sensor based on Vernier Effect. *Sensors* **2018**, *18*, 3677. [[CrossRef](#)]
7. Campanella, C.E.; Malara, P.; Campanella, C.M.; Giove, F.; Dunai, M.; Passaro, V.M.N.; Gagliardi, G. Mode-splitting cloning in birefringent fiber Bragg grating ring resonators. *Opt. Lett.* **2016**, *41*, 2672–2675. [[CrossRef](#)] [[PubMed](#)]
8. Campanella, C.E.; Leonardi, F.D.; Mastronardi, L.; Malara, P.; Gagliardi, G.; Passaro, V.M.N. Investigation of refractive index sensing based on Fano resonance in fiber Bragg grating ring resonators. *Opt. Express* **2015**, *23*, 14301–14313. [[CrossRef](#)] [[PubMed](#)]
9. Chen, F.; Zhang, H.; Sun, L.; Li, J.; Yu, C. Temperature tunable Fano resonance based on ring resonator side coupled with a MIM waveguide. *Opt. Laser Technol.* **2019**, *116*, 293–299. [[CrossRef](#)]
10. Mandal, S.; Dasgupta, K.; Basak, T.K.; Ghosh, S.K. A generalized approach for modeling and analysis of ring-resonator performance as optical filter. *Opt. Commun.* **2006**, *1*, 97–104. [[CrossRef](#)]
11. Limonov, M.F.; Rybin, M.V.; Poddubny, A.N.; Kivshar, Y.S. Fano resonances in photonics. *Nat. Photonics* **2017**, *11*, 543–554. [[CrossRef](#)]
12. Ben Hassen, R.; Caucheteur, C.; Delchambre, A. FBGs temperature sensor for electrosurgical knife subject to high voltage and high-frequency current. In *Optical Sensing and Detection VI, Proceedings of the SPIE PHOTONICS EUROPE, Online, 6–10 April 2020*; SPIE: Bellingham, WA, USA, 2020; Volume 11354.
13. Pinet, É.; Ellyson, S.; Borne, F. Temperature Fiber-Optic Point Sensors: Commercial Technologies and Industrial Applications. *Inf. MIDEA* **2010**, *40*, 275–286.
14. Eom, J.; Park, C.-J.; Lee, B.H.; Lee, J.-H.; Kwon, I.-B.; Chung, E. Fiber optic Fabry-Perot pressure sensor based on lensed fiber and polymeric diaphragm. *Sens. Actuators A Phys.* **2015**, *225*, 25–32. [[CrossRef](#)]
15. Liang, H.; Jia, P.; Liu, J.; Fang, G.; Li, Z.; Hong, Y.; Liang, T.; Xiong, J. Diaphragm-Free Fiber-Optic Fabry-Perot Interferometric Gas Pressure Sensor for High Temperature Application. *Sensors* **2018**, *18*, 1011. [[CrossRef](#)] [[PubMed](#)]
16. Ledyankin, M.A.; Mikhailov, S.A.; Nedel'ko, D.V.; Agliullin, T.A. Implementation of the Radiophotonic Method for Measuring Blade Deformations of a Helicopter Main Rotor Model. *Russ. Aeronaut.* **2020**, *63*, 767–770. [[CrossRef](#)]
17. Lawson, N.J.; Correia, R.; James, S.W.; Partridge, M.; Staines, S.E.; Gautrey, J.E.; Garry, K.P.; Holt, J.C.; Tatam, R.P. Development and application of optical fibre strain and pressure sensors for in-flight measurements. *Meas. Sci. Technol.* **2016**, *27*, 104001. [[CrossRef](#)]
18. Kuznetsov, A.A.; Lipatnikov, K.A.; Nureev, I.I.; Morozov, O.G.; Sakhabutdinov, A.J. Fiber-optic sensors for complex monitoring of traction motors. In Proceedings of the Journal of Physics: Conference Series; Institute of Physics Publishing: Bristol, UK, 2019; Volume 1327, p. 012034.
19. Morozov, O.G.; Nureev, I.I.; Kuznetsov, A.A.; Artemiev, V.I. Smart Photonic Carbon Brush: FBG Length as Sensing Parameter. *J. Phys. Conf. Ser.* **2018**, *999*, 012017. [[CrossRef](#)]
20. Wang, C.; Yao, J. Fiber Bragg gratings for microwave photonics subsystems. *Opt. Express* **2013**, *21*, 22868–22884. [[CrossRef](#)]
21. Qin, C.; Zhao, J.; Jiang, B.; Yang, D. Sub-pixel algorithms on linear-array detector grating spectrometer. In *Advanced Sensor Systems and Applications V, Proceedings of the PHOTONICS ASIA, Beijing, China, 5-7 November 2012*; Culshaw, B., Liao, Y., Wang, A., Bao, X., Fan, X., Eds.; SPIE: Bellingham, WA, USA, 2012; p. 85610N.
22. Bodendorfer, T.; Muller, M.S.; Hirth, F.; Koch, A.W. Comparison of different peak detection algorithms with regards to spectrometric fiber Bragg grating interrogation systems. In Proceedings of the 2009 International Symposium on Optomechatronic Technologies, Istanbul, Turkey, 21–23 September 2009; pp. 122–126.
23. Sakhabutdinov, A.Z.; Nureev, I.I.; Morozov, O.G. Clarification of the central wavelength FBG position in a poor signal-to-noise ratio conditions. *Phys. Wave Process. Radio Syst.* **2015**, *18*, 98–102. (In Russian)
24. Anfinogentov, V.; Karimov, K.; Kuznetsov, A.; Morozov, O.G.; Nureev, I.; Sakhabutdinov, A.; Lipatnikov, K.; Hussein, S.M.R.H.; Ali, M.H. Algorithm of FBG Spectrum Distortion Correction for Optical Spectra Analyzers with CCD Elements. *Sensors* **2021**, *21*, 2817. [[CrossRef](#)]

25. Deepa, S.; Das, B. Interrogation techniques for π -phase-shifted fiber Bragg grating sensor: A review. *Sens. Actuators A Phys.* **2020**, *315*, 112215. [[CrossRef](#)]
26. Agrawal, G.P.; Radic, S. Phase-shifted fiber Bragg gratings and their application for wavelength demultiplexing. *IEEE Photonics Technol. Lett.* **1994**, *6*, 995–997. [[CrossRef](#)]
27. Dai, B.; Gao, Z.; Wang, X.; Kataoka, N.; Wada, N. Performance comparison of $0/\pi$ - and $\pm\pi/2$ -phase-shifted superstructured Fiber Bragg grating encoder/decoder. *Opt. Express* **2011**, *19*, 12248–12260. [[CrossRef](#)] [[PubMed](#)]
28. Morozov, O.G.; Nureev, I.I.; Sahabuddinov, A.Z.; Gubaidullin, R.R.; Morozov, G.A. Problem of fano resonance characterization in ring π -shift fiber bragg grating biosensors. In Proceedings of the 2019 Systems of Signal Synchronization, Generating and Processing in Telecommunications (SYNCHROINFO), Yaroslavl, Russia, 1–3 July 2019; pp. 1–6.
29. Xu, O.; Zhang, J.; Yao, J. High speed and high resolution interrogation of a fiber Bragg grating sensor based on microwave photonic filtering and chirped microwave pulse compression. *Opt. Lett.* **2016**, *41*, 4859–4862. [[CrossRef](#)] [[PubMed](#)]
30. Ricchiuti, A.L.; Barrera, D.; Sales, S.; Thévenaz, L.; Capmany, J. Long Weak FBG Sensor Interrogation Using Microwave Photonics Filtering Technique. *IEEE Photonics Technol. Lett.* **2014**, *26*, 2039–2042. [[CrossRef](#)]
31. Negri, L.; Nied, A.; Kalinowski, H.; Paterno, A. Benchmark for Peak Detection Algorithms in Fiber Bragg Grating Interrogation and a New Neural Network for its Performance Improvement. *Sensors* **2011**, *11*, 3466–3482. [[CrossRef](#)] [[PubMed](#)]
32. An, Y.; Wang, X.; Qu, Z.; Liao, T.; Nan, Z. Fiber Bragg grating temperature calibration based on BP neural network. *Optik* **2018**, *172*, 753–759. [[CrossRef](#)]
33. Zimmermann, A.C.; Veiga, C.L.N.; Encinas, L.S. Unambiguous Signal Processing and Measuring Range Extension for Fiber Bragg Gratings Sensors Using Artificial Neural Networks—A Temperature Case. *IEEE Sens. J.* **2008**, *8*, 1229–1235. [[CrossRef](#)]
34. Paterno, A.S.; Silva, J.C.C.; Milczewski, M.S.; Arruda, L.V.R.; Kalinowski, H.J. Radial-basis function network for the approximation of FBG sensor spectra with distorted peaks. *Meas. Sci. Technol.* **2006**, *17*, 1039–1045. [[CrossRef](#)]
35. Orr, M.J.L. Regularization in the Selection of Radial Basis Function Centers. *Neural Comput.* **1995**, *7*, 606–623. [[CrossRef](#)]
36. Kahandawa, G.C.; Epaarachchi, J.A.; Wang, H.; Followell, D.; Birt, P. Use of fixed wavelength Fibre-Bragg Grating (FBG) filters to capture time domain data from the distorted spectrum of an embedded FBG sensor to estimate strain with an Artificial Neural Network. *Sens. Actuators A Phys.* **2013**, *194*, 1–7. [[CrossRef](#)]
37. Jiang, H.; Zeng, Q.; Chen, J.; Qiu, X.; Liu, X.; Chen, Z.; Miao, X. Wavelength detection of model-sharing fiber Bragg grating sensor networks using long short-term memory neural network. *Opt. Express* **2019**, *27*, 20583. [[CrossRef](#)]
38. Kokhanovskiy, A.; Shabalov, N.; Dostovalov, A.; Wolf, A. Highly Dense FBG Temperature Sensor Assisted with Deep Learning Algorithms. *Sensors* **2021**, *21*, 6188. [[CrossRef](#)] [[PubMed](#)]
39. Agliullin, T.; Anfinogentov, V.; Morozov, O.; Sakhabutdinov, A.; Valeev, B.; Niyazgulyeva, A.; Garovov, Y. Comparative Analysis of the Methods for Fiber Bragg Structures Spectrum Modeling. *Algorithms* **2023**, *16*, 101. [[CrossRef](#)]
40. Erdogan, T. Fiber grating spectra. *J. Light. Technol.* **1997**, *15*, 1277–1294. [[CrossRef](#)]
41. White, B.W.; Rosenblatt, F. Principles of Neurodynamics: Perceptrons and the Theory of Brain Mechanisms. *Am. J. Psychol.* **1963**, *76*, 705. [[CrossRef](#)]
42. Amari, S. Backpropagation and stochastic gradient descent method. *Neurocomputing* **1993**, *5*, 185–196. [[CrossRef](#)]
43. Nesterov, Y. *Introductory Lectures on Convex Optimization*; Applied Optimization; Springer: Boston, MA, USA, 2004; Volume 87, ISBN 978-1-4613-4691-3.
44. Kingma, D.P.; Ba, J. Adam: A Method for Stochastic Optimization. In Proceedings of the 3rd International Conference for Learning Representations, San Diego, CA, USA, 7–9 May 2015.
45. Chen, R.; He, J.; Xu, X.; Wu, J.; Wang, Y.; Wang, Y. High-Quality Fiber Bragg Gratings Inscribed by Femtosecond Laser Point-by-Point Technology. *Micromachines* **2022**, *13*, 1808. [[CrossRef](#)]
46. Marshall, G.D.; Williams, R.J.; Jovanovic, N.; Steel, M.J.; Withford, M.J. Point-by-point written fiber-Bragg gratings and their application in complex grating designs. *Opt. Express* **2010**, *18*, 19844–19859. [[CrossRef](#)]

Disclaimer/Publisher’s Note: The statements, opinions and data contained in all publications are solely those of the individual author(s) and contributor(s) and not of MDPI and/or the editor(s). MDPI and/or the editor(s) disclaim responsibility for any injury to people or property resulting from any ideas, methods, instructions or products referred to in the content.